Korean J. Chem. Eng., 38(10), 2157-2170 (2021)
DOI: 10.1007/s11814-021-0856-7

pISSN: 0256-1115
eISSN: 1975-7220

Synthesis of super-absorbent poly(AN)-g-starch composite hydrogel and its modelling for aqueous sorption of cadmium ions

Ali Hashem*,†, Chukwunonso Onyeka Aniagor,†, Mohamed Abdel-Fattah Afifi*, Ashraf Abou-Okeil*, and Sayed Hussein Samaha*****

*Textile Research Division, National Research Centre, Dokki, Cairo, Egypt
**Department of Chemical Engineering, Nnamdi Azikiwe University, P.M.B. 5025, Awka, Nigeria
***Textile Metrology Department, National Institute of Standards, Tersa Street, El-Haram, Giza, Egypt
(*Received 5 March 2021 • Revised 24 April 2021 • Accepted 22 May 2021*)

Abstract−To entrench heavy metal chelation functional groups, native corn starch was grafted with acrylonitrile and subsequently hydrolyzed (using sodium hydroxide) to produce chemically crosslinked superabsorbent hydrogels (SAHs) of three-dimensional hydrophilic polymeric networks. SAHs demonstrated fast swelling and superabsorbent properties, with a swelling capacity of 612 g water/g SAHs. Due to the usefulness of equilibrium and kinetic data for elucidating the nature of adsorbate-adsorbent interaction, the adsorption study was extensively modelled using selected nonlinear isotherm and kinetics models. The Toth and intraparticle diffusion models satisfactorily predicted the isotherm and kinetic data, respectively, while the dominance of the metal complexation mechanism was asserted in the study. Meanwhile, the metal ion uptake by SAHs occurred at a fast equilibration time of 20 min. Furthermore, the adsorbent's instrumental characterization (scanning electron microscopy, SEM; Energy dispersion X-ray, EDX; X-ray diffraction, XRD and Fourier-transform infrared spectroscopy, FTIR) result confirmed that SAHs possesses the desired metal chelation properties. Thus, the potential application of the developed SAHs as biosorbent in the decontamination of the heavy metal-laden stream was explicitly demonstrated in the study.

Keywords: Starch, Superabsorbent Hydrogel, Adsorption, Cadmium (II) Ion, Isotherm, Kinetics

INTRODUCTION

Starch is the most abundant storage polysaccharide in plants and exists as granules in the chloroplast of green leaves and the amyloplast of seeds, pulses, and tubers [1]. Its main structural components (amylose and amylopectin) are composed of several monosaccharides or glucose molecules joined together with α-D-(1-4) and/or α-D-(1-6) linkages [2]. The relative proportion of these components remains a function of the starch source, its molecular order and the polysaccharide crystallinity [3].

Starch finds extensive application in process chemistry due to its relative abundance, renewable nature, cost-effectiveness and a degree of flexibility which is comparable to that of natural tissues [4]. Meanwhile, the absence of relevant functional groups on native starch has been reported as a major drawback for heavy metal sorption application [5-7]. Various surface functionalization approaches, such as etherification, crosslinking, esterification, grafting, and decomposition reactions (such as acid and enzymatic hydrolysis), are often adopted for entrenching the required functional groups [7-14]. For instance, starch with abundant hydroxyl groups is preferable for hydrogel synthesis [15] and the hydroxyl content of native starch can be improved via either etherification or copolymerization grafting.

The negative impact of heavy metal pollution/contamination (even at trace level) on the ecosystem and living organisms has been extensively reported [7,9,16-21]. However, due to its high adsorption capacity, the existence of abundant surface functional groups and seamless reusability, copolymerized polysaccharide-based hydrogels have received great research attention. To this end, different types of natural polysaccharide graft copolymers were previously applied [22-27] as adsorbents for heavy metal sequestration.

In this study, a chemically crosslinked superabsorbent hydrogel (SAH) of three-dimensional hydrophilic polymeric networks was synthesized from corn starch and subsequently applied for aqueous cadmium (II) uptake. The polymeric network of the SAHs is composed of acrylonitrile copolymer, with substantial water absorption capacity [28]. The main hydrolysis product of the polar nitrile (CN) groups of the acrylonitrile monomer ($CONH_2$ groups) provides better binding interaction with the starch molecule in the presence of an appropriate initiator [29]. Similarly, the attachment of the polar groups of acrylonitrile to the starch polymer backbone enhances the hydrogels' water absorption capacity and also establishes stable network chains which mitigate the hydrogel dissolution [4]. The synthesis of such superabsorbent polymer based on the graft copolymers of polyacrylonitrile (PAN) onto starch was pioneered by a group at the Northern Regional Research Laboratory, US Department of Agriculture [30,31].

The effect of certain process variables on the SAHs adsorption capacity, as well as the process equilibrium and kinetics modelling, was extensively investigated in the study. Equilibrium modelling was

†To whom correspondence should be addressed.
E-mail: alihashem2000@yahoo.com, co.aniagor@unizik.edu.ng

applied for the establishment of the equilibrium correlation, which is necessary for defining the appropriateness or otherwise of a given adsorbent [32]. It also helps to predict such adsorbent behavior when subjected to varying experimental conditions. Furthermore, information obtained from proper adsorption isotherms evaluation could be beneficial in the design of an industrial adsorption process [33]. Similarly, the kinetics studies using different classical nonlinear models are an important approach for probing the controlling mechanism of the adsorption system. The SAHs structural, morphological and textural characteristics were elucidated by Fourier transform infrared spectroscopy (FTIR), scanning electron microscopy (SEM), energy-dispersive X-ray spectroscopy (EDS) and X-ray diffraction (XRD).

MATERIALS AND METHODS

1. Materials

Corn starch was kindly supplied by the Egyptian Starch and Glucose Manufacturing Company, Cairo, Egypt. All other reagents utilized in this work, polyacrylonitrile, ammonium cerium (IV) nitrate (CAN), cadmium acetate, caustic soda, ethylenediaminetetraacetic acid (EDTA), nitric acid, acetic acid, acetone, methanol, and ethyl alcohol were all laboratory grade chemicals, supplied by Merck, Germany.

2. Methods

2-1. Graft Procedure

The procedure for the polyacrylonitrile [Poly (AN)]-starch composite grafting was adopted from Abdel-Halim [34], with slight modifications. The procedure involves the gelatinization of a known mass of dried corn starch in a suitable (enough to form a gel) volume of water contained in a 100 mL Erlenmeyer flask. The mixture was heated to and maintained at 85 °C for 30 min using a thermostatic water bath. Afterwards, a specific volume of acrylonitrile, as well as a binary mixture of freshly prepared ammonium cerium (IV) nitrate and 1 N HNO_3 was introduced into the flask containing the already cooled (30-33 °C) gelatinized starch. The set-up was left to stand for a predetermined duration at ambient temperature (30±3 °C) and continuous stirring (150 rpm).

The homopolymer was eliminated for the poly (AN)-starch graft copolymer through precipitation of the later in N, N- dimethylformamide (DMF). Consequent upon centrifugation (at 4,000 rpm for 10 min), the desired precipitate was obtained, washed with deionized water and then oven-dried at 50 °C to constant dry weight. The poly (AN)-starch graft copolymer yield was estimated (after the extraction of the associated homopolymer) from its nitrogen content as expressed in Eq. (1) [20]. Meanwhile, the % nitrogen content was obtained following the micro-Kjeldahl method [10].

$$\% \text{ Graft yield} = \frac{\left[\frac{(N\ (\%)*53)}{14}*100\right]}{\left[\frac{100-(N\ (\%)*53)}{14}\right]} \quad (1)$$

NB: 53 and 14 is the molecular weight of acrylonitrile and Nitrogen (N), respectively.

2-2. Hydrogel Synthesis

1.0 g of poly (AN)-starch composite was treated with 10 mL of 0.7 N NaOH in a loosely stoppered (to permit ammonia evolution) flask. The mixture was mechanically stirred using a thermostatic magnetic stirrer (at 150 rpm and 95 °C) until the saponification reaction was completed, as indicated by a solution color change from deep red to light yellow. Afterwards, the content of the loosely stoppered flask was initially dispersed in a predetermined volume of methanol (coupled with stirring for 5 min) and the entire mixture was subsequently charged into an excess volume of ethanol. The precipitate so obtained (desired adsorbent) was washed with acetic acid acidified ethanol until pH 8.0, filtered off, oven-dried (60 °C, 3 h) to obtain the superabsorbent hydrogels (SAHs), which were further ground to a uniform particle size of ≤150 μm).

2-3. Hydrogel Swelling Capacity Measurement

In the procedure, 1.0 g of the SAHs was impregnated in distilled water (100 mL) at ambient temperature (30±3 °C). The SAHs were left in the water until the attainment of the water absorption saturation point. Subsequently, the fully swollen SAHs were recovered as filtrate from the water, drained and reweighed. The swelling capacity of the superabsorbent hydrogel (SAHs) was evaluated from Eq. (2) [20,34] and expressed in grams of water/grams of dry SAHs.

$$\text{Seelling capacity}\left(\frac{g}{g}\right) = \frac{M_1 - M_2}{M_1} \quad (2)$$

where M_1 and M_2 are the masses of swollen SAHs and dry SAHs.

3. Sample Instrumental Characterization

The surface functional groups, morphology and elemental distribution mapping of the synthesized adsorbent was identified using Fourier transform infrared spectroscopy (Perkin-Elmer Spectrum 1000 spectrophotometer), scanning electron microscopy (TESCAN CE VEGA 3 SBU: 117-0195- Czech Republic) and Energy-dispersive X-ray (Dispersive X-ray fluorescence spectrometer, Oxford Instruments). The surface crystallinity of the samples was obtained using X-ray diffraction, XRD (XPERT - PRO - PANalytical - Netherlands).

4. Adsorption Experiments

A specific amount of SAHs (0.03 g) was contacted with 100 mL of a Cd (II) ion solution in a 125 mL Erlenmeyer flask. The solution pH was rightly tuned using either 0.1 M HNO_3 or 0.1 M NaOH. After a certain period of agitation (at 150 rpm, 30 °C), the mixture was filtered using Whatman No. 41 paper to separate the adsorbent and metal ion solution. The variation in the Cd (II) ion concentration was obtained from the direct titration with a standard EDTA solution. Meanwhile, the relevant parameters (amount adsorbed at any instant, q_t and equilibrium, q_e, removal efficiency, R.E %) derivable from the adsorption experiment were evaluated with Eqs. (3)-(5).

$$q_e = \frac{(C_o - C_e)V}{W} \quad (3)$$

$$q_t = \frac{(C_o - C_t)V}{W} \quad (4)$$

$$RE\ (\%) = \frac{C_o - C_e}{C_o} \cdot 100\% \quad (5)$$

where C_o=Initial Cd (II) concentration (mg L^{-1}), C_e=Cd (II) concentration at equilibrium (mg L^{-1}), W=Mass of SAHs (g), V= volume of Cd (II) solution used (L).

5. Adsorption Kinetic Modelling

5-1. Pseudo-first-order (PFO) Model

PFO [35] assumes that solute adsorption follows a first-order reaction mechanism, as well as an inverse relationship between the adsorption rate constant (k_1) and adsorbate concentration. The nonlinear form of the PFO model is presented in Eq. (6).

$$q_t = q_e\,[1-\exp(-k_1 t)] \tag{6}$$

5-2. Pseudo-second-order (PSO) Model

According to PSO [36] model assumptions, there is a proportional relationship between the adsorption rate and adsorption sites on the adsorbent. The model can also provide information on the adsorbents' adsorption capacity. The PSO nonlinear equation is expressed as Eq. (7).

$$q_t = \frac{k_2 * q_e^2 * t}{(1 + k_2 * t)} \tag{7}$$

5-3. Elovich Model

The application of the Elovich model [7,10,21] helps to elucidate the chemisorption process, as well as predicts the extent of mass transfer, surface diffusion and activation energy of the system. The models' nonlinear equation is expressed as Eq. (8).

$$q_t = \beta * \ln(\alpha\beta t) \tag{8}$$

5-4. Intra-particle Diffusion Model

Since adsorption involves the mass transfer of solute, this model is employed in identifying the governing mechanism in an adsorption system. The model was postulated by Weber et al. [37] and the nonlinear equation is presented in Eq. (9). The magnitude of the model's c-value explains the effect of the boundary layer during adsorption. The greater the magnitude of the c-value, the larger the boundary layer thickness.

$$q_t = k_{id} t^{0.5} \tag{9}$$

5-5. Bangham Model

The dominance of pore diffusion as the sole mechanism in a given adsorption process is investigated using Bangham's kinetic model [38,39]. The model equation is expressed as Eq. (10).

$$q_t = q_e[1-\exp(-k_b t^n)] \tag{10}$$

6. Adsorption Isotherm Modelling

6-1. Langmuir Model

This is an empirical model that postulates monolayer sorption, occurring at an exact adsorption site and devoid of adsorbent-adsorbate lateral interaction [40]. The model is also useful for quantifying adsorbent uptake performance [41]. The nonlinear Langmuir model and dimensionless constant, (separation factor, R_L) are expressed as Eqs. (11)-(12) [41].

$$q_e = \frac{q_m k_L C_e}{1 + k_L C_e} \tag{11}$$

$$R_L = \frac{1}{1 + K_L C_o} \tag{12}$$

where $R_L>1$, $R_L=1$, $R_L=0$ and $0<R_L<1$ implies unfavorable, linear, irreversible and favorable nature of the adsorption process, respectively.

6-2. Freundlich Model

This model is well suited for multilayer adsorption onto heterogeneous adsorbent surfaces, where adsorption heat is unevenly distributed [42]. The model constant 'n_F' provides information on the surface heterogeneity. Similarly, chemisorption and increased surface heterogeneity predominate in an adsorption system when the 'n_F'-value is below unity. The nonlinear Freundlich equation is expressed as Eq. (13).

$$q_e = K_F (C_e)^{\frac{1}{n_F}} \tag{13}$$

6-3. Dubinin-Radushkevich (D-R) Model

As an empirical model, the Dubinin-Radushkevich isotherm [43] effectively relates the mechanism of heterogeneous surface adsorption with Gaussian distribution of energy [44,45]. The model term 'E', which denotes the mean free energy and is evaluated from Eq. (14), offers a distinction between physical (E<8 kJ/mol) and chemical adsorption [46]. The D-R model equation is shown in Eq. (15).

$$E = \frac{1}{\sqrt{2\beta_D}} \tag{14}$$

$$q_e = q_D * \exp\left\{-B_D\left[RT\left(1+\frac{1}{C_e}\right)\right]^2\right\} \tag{15}$$

6-4. Temkin Model

The Temkin model [47] parameters effectively correlate the interaction between a given adsorbent and adsorbate, with a characteristic even binding energy distribution. Having ignored extreme concentration values, the model postulates a linear (and not logarithmic) decrease in adsorption heat with surface coverage. The model equation is presented in Eq. (16).

$$q_e = \frac{RT}{b_T}\ln(K_T C_e) \tag{16}$$

6-5. Halsey Model

Like the Freundlich model, the Halsey isotherm assumes the occurrence of heterogeneous multilayer adsorption near the adsorbent surface boundaries [48,49]. The model is expressed mathematically as Eq. (17) [50].

$$q_e = \exp\left(\frac{\ln K_{Ha} - \ln C_e}{n_{Ha}}\right) \tag{17}$$

6-6. Sips Model

Sip [51] is a hybrid model which bridges the Langmuir and Freundlich models. The model can predict heterogeneous surface adsorption while taking care of the associated limitations of the Freundlich model at high adsorbate concentration. The Sip model approaches the Freundlich and the Langmuir models at low and high adsorbate concentrations, respectively. Its nonlinear mathematical expression is shown in Eq. (18).

$$q_e = \frac{K_s * C_e^{\beta_1}}{1 + a_s * C_e^{\beta_1}} \tag{18}$$

6-7. Khan Model

Khan isotherm [16] is generally applied in cases of adsorbate

Table 1. The applied goodness-of-fit models

Error function	Equation	References
Average Relative Error (ARE)	$ARE = \sum_{i=1}^{n} \left\| \frac{(q_e)_{exp.} - (q_e)_{calc.}}{(q_e)_{exp.}} \right\|$	[62]
Average Percentage Error (APE)	$APE\% = \frac{\sum_{i=1}^{N} \left\| [((q_e)_{exp.} - (q_e)_{calc.})/q_{exp.}] \right\|}{N} \times 100$	[63]
Sum Squares Error (ERRSQ/SSE)	$ERRSQ = \sum_{i=1}^{n} [(q_e)_{calc.} - (q_e)_{exp.}]^2$	[57]
Hybrid Fraction Error Function (Hybrid)	$Hybrid = \frac{100}{n-p} \sum_{i=1}^{n} \left[\frac{((q_e)_{exp.} - (q_e)_{calc.})^2}{(q_e)_{exp.}} \right]_i$	[64]
Marquardt's Percent Standard Deviation (MPSD)	$MPSD = \sqrt[100]{\frac{1}{n-p} \sum_{i=1}^{n} \left[\frac{((q_e)_{exp.} - (q_e)_{calc.})}{(q_e)_{exp.}} \right]^2}$	[62]
Nonlinear chi-square test (χ^2)	$\chi^2 = \sum \frac{(q_{e.\,exp} - q_{e.\,theoretical})^2}{q_{e.\,theoretical}}$	[65]
Coefficient of determination (R^2)	$R^2 = \frac{\sum_{i=1}^{n} (q_{e,\,calc} - \overline{q_{e,\,exp}})^2}{\sum_{i=1}^{n} (q_{e,\,calc} - \overline{q_{e,\,exp}})^2 + \sum_{i=1}^{n} (q_{e,\,calc} - q_{e,\,exp})^2}$	[60]

and pure solutions. The corresponding model constant and exponent are denoted as 'b_K' and 'a_K', respectively. The nonlinear Khan equation is expressed as Eq. (19).

$$q_e = \frac{q_{mK} * b_K * C_e}{(1 + b_K * C_e)^{a_K}} \tag{19}$$

6-8. Toth Model

Toth isotherm model [52], efficiently describes heterogeneous surface adsorption and also offers an improvement on the fitting of the Langmuir model by satisfying the lower and upper boundaries of adsorbate concentration [40]. The model postulates uneven adsorption energy distribution, with lower adsorption site energy, which is often lower than the peak energy values [53]. The model is expressed mathematically as Eq. (20).

$$q_e = \frac{k_T * C_e}{(a_T + C_e)^{t^{-1}}} \tag{20}$$

6-9. Hill Model

The Hill isotherm is useful for describing homogeneous surface adsorption, as it assumes cooperative monolayer adsorption on non-uniform sites of the same adsorbent [54]. The model's nonlinear equation is shown in Eq. (21).

$$q_e = \frac{q_{mH} C_e^{n_H}}{K_H + C_e^{n_H}} \tag{21}$$

6-10. Redlich-Peterson Model

Redlich-Peterson isotherm [55], a three parameter empirical model is a hybrid version of Langmuir and Freundlich models [56]. The numerator and the denominator of the model equation contain a term that is linearly dependent on adsorbate concentration and an exponential function, respectively [57]. Due to the aforementioned characteristics, the R-P equation applies to both homogeneous and heterogeneous adsorption systems [58] and exhibits Freundlich and Langmuir model characteristics at high and low adsorbate concentrations, respectively [59]. The model equation is expressed as Eq. (22).

$$q_e = \frac{K_{RP} C_e}{1 + \alpha_{RP} (C_e)^g} \tag{22}$$

7. Error Functions

For nonlinear isotherm and kinetic models, the minimization of error variance between the predicted and experimental data form the basis for the adoption of a goodness-of-fit model (GOFm) [60,61]. In this study, six error functions and the coefficient of determination (R^2), as presented in Table 1 were applied for evaluating the goodness of the respective isotherm and kinetic model fits. The lower the error values for a given isotherm or kinetic model, the better the model fit, while a larger R^2-value implies a better model fit.

RESULTS AND DISCUSSION

1. Mechanism of SAHs Synthesis

The gelatinating, copolymerization grafting and saponification (hydrogel formation) of the corn starch afforded the superabsorbent hydrogels (SAHs) adsorbent used in the study. The mechanism involved during the SAHs synthesis is presented in Eqs. (23)-(24). The heat treatment (see section 2.2.1) enhanced the initial gelatinization of the starch molecules, while the introduction of acrylonitrile (in the presence of CAN initiator) successfully yielded poly (AN)-starch graft copolymer via the formation of homopolymer and starch oxidation as shown in Eq. (23). As expressed in Eq. (24), the saponification of the poly (AN)-starch graft copolymer (via reaction with sodium hydroxide) yielded the desired super-

Table 2. Characteristics of SAHs

N % in poly (AN)-starch graft copolymer	N % in SAHs	Swelling capacity (g/g)
10.44	2.58	612.0

absorbent hydrogels (SAHs).

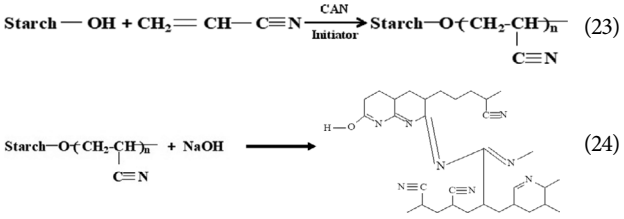

2. SAHs Characterization Results

Some of the SAHs characteristics that are relevant to its heavy metal sorption capacity is shown in Table 2. It was observed that the % nitrogen content decreased after the saponification reaction; hence the polymer composite recorded a much higher % nitrogen content than the SAHs. The observed decline in the SAHs % nitrogen is due to the depletion of the cyano groups of the poly (AN)-starch graft copolymer, which are involved in the formation of nitrogen-based (amide, nitrile, etc) groups and sodium carboxylate salt. Meanwhile, the carboxylate salt was eliminated in the precipitation stage of SAHs synthesis (see section 2.2.2).

The swelling capacity of SAHs was recorded as 612 g water/g SAHs as shown in Table 2. The high water absorption is well related to the gelatinization process and subsequent formation of the copolymer graft. The gelatinization effect caused substantive physical modification to the starch structure (like the disordering of the starch molecules, increase in starch chain free volume) [10], while the graft formation improved the SAHs structural network through increased crosslinking [34].

3. Instrumental Characterization

3-1. Surface Chemistry

The results from the FTIR spectroscopic analyses of the native corn starch, poly(AN)-g-starch, superabsorbent hydrogel (SAHs) and cadmium-loaded SAHs are presented in Fig. 1. The different spectra depict identical signature peaks for starch molecules at the broadband around 3,404 cm^{-1} (represents H-bonded OH/NH stretch)

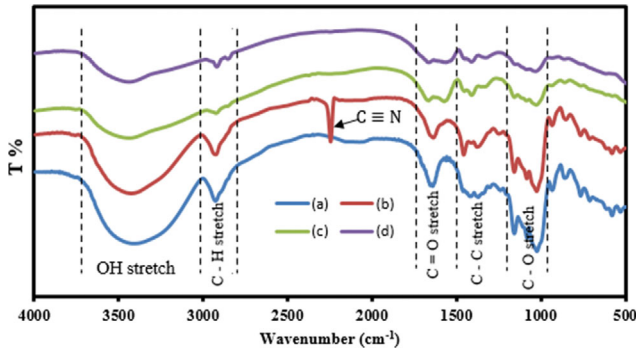

Fig. 1. FTIR spectra for (a) native corn starch, (b) poly(AN)-g-starch, (c) hydrolyzed poly(AN)-g-starch, (d) Cd (II)- loaded-hydrolyzed poly(AN)-g-starch.

and the peak around 2,926 cm^{-1} (represents C-H stretch). Besides, other common peaks exist around 1,720-1,550 cm^{-1}, 1,400-1,200 cm^{-1} and those around 1,150 cm^{-1} which are attributed to the amide/carboxylate C=O stretch, C-C or C-N stretch and C-O stretch [66]. Few differences were observed upon the comparison of the different spectra. For instance, the starch C-H stretch diminished after hydrogel formation and subsequent sorption of cadmium (II) ion (compare spectra lines (b), (c) and (d) of Fig. 1). The same case of absorption peak shrinkage was also observed at the C=O stretch, C-C stretch and C-O stretch groups. Notably, a prominent peak that was attributed to the nitrile (C≡N) group was identified around 2,245 cm^{-1} in the poly(AN)-g-starch spectra. The presence of this nitrile group and the weak symmetrical C-N stretching at 1,390 cm^{-1} affirmed the success of the copolymer grafting. Furthermore, the nitrile group which was introduced during grafting subsequently disappeared after the saponification reaction.

3-2. Surface Morphology

The structural properties of the native corn starch, poly(AN)-g-starch, superabsorbent hydrogel (SAHs) and cadmium-loaded SAHs are presented in Fig. 2. All the SEM images depict the resemblance of a wrinkled amorphous polymeric matrix with fibrous interconnections. Grafting modified the morphology of the native starch (Fig. 2(a)) to depict better surface aggregated patches (Fig. 2(b)). Also, slight evidence for the partial collapsing of the starch polymeric networks was observed, probable due to the heat treatment and infusion of nitrogen groups. The saponification process towards the formation of starch hydrogel further aggregated the surface amorphous matrix into a more loosely bound biofilm-like agglomerate, with superior surface roughness and porosity (Fig. 2(c)). The improved surface roughness and porosity could have occurred as a result of the precipitation, which eliminated certain solubilized low molecular weight carboxylates during SAHS synthesis. The comparison of Fig. 2(c) and Fig. 2(d) shows that the changes occurring due to Cd (II) ion adsorption had no significant impact on the SAHs morphology, an indication of the adsorbent's robustness and stability.

3-3. Elemental Distribution Mapping

Since no significant morphological distinction was observed in the post adsorption SEM image as expressed in section 3.3.2, energy dispersion X-ray (EDX) analysis was conducted to confirm the actual presence of the adsorbed cadmium ions and their percentage of deposition. The post-adsorption SEM-EDX elemental mapping, containing the SEM images and percentage elemental distribution, is presented in Fig. 3. In addition to the confirmation of the presence of adsorbed Cd (II) ion, the presence of other elements with varying % compositions was also observed. Notably, a limited % presence of nitrogen element was observed. This development further confirmed the transformation of some of the cyano groups of the poly (AN)-starch graft copolymer, which was earlier asserted in section 3.2. Also, the oxygen element which provided some metal complexation sites (see Scheme 1) was among the dis-

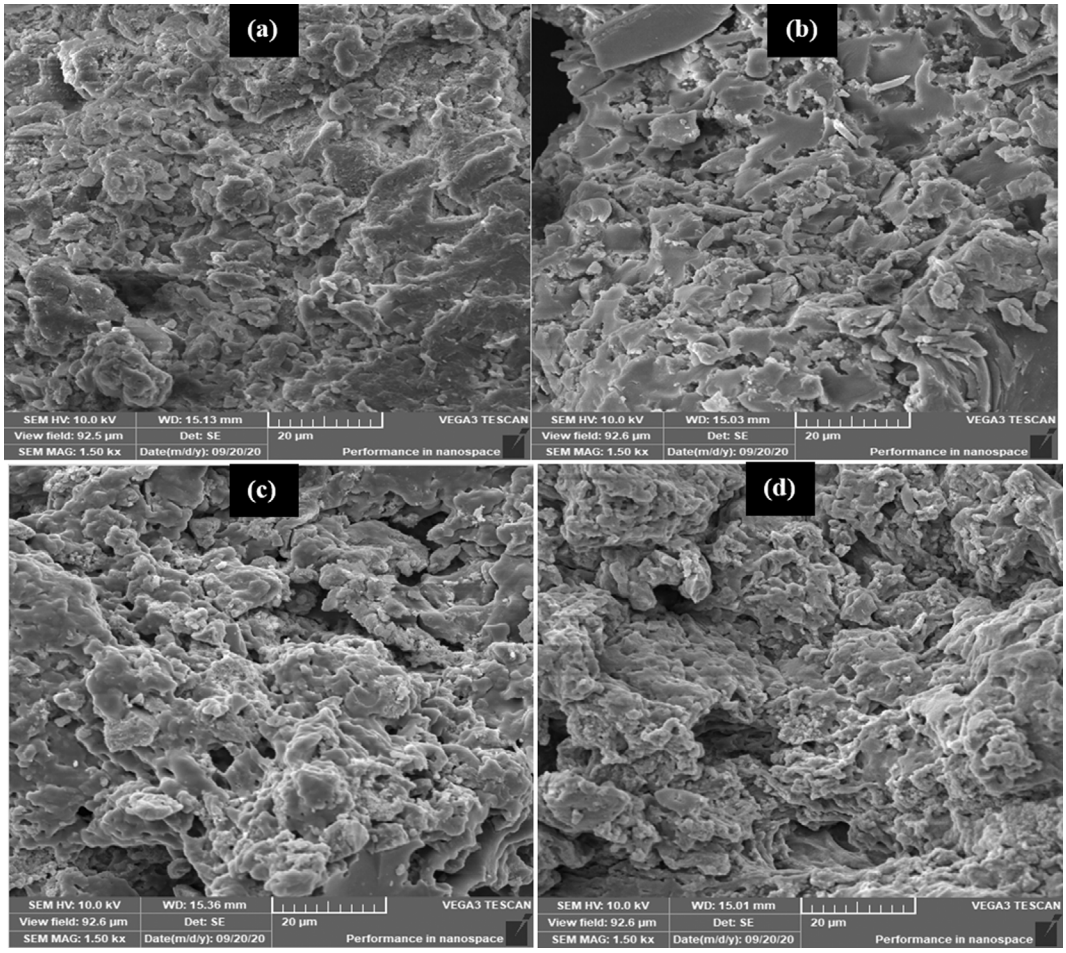

Fig. 2. SEM images of (a) native corn starch, (b) poly(AN)-g-starch, (c) hydrolyzed poly(AN)-g-starch, (d) Cd(II)- loaded-hydrolyzed poly(AN)-g-starch.

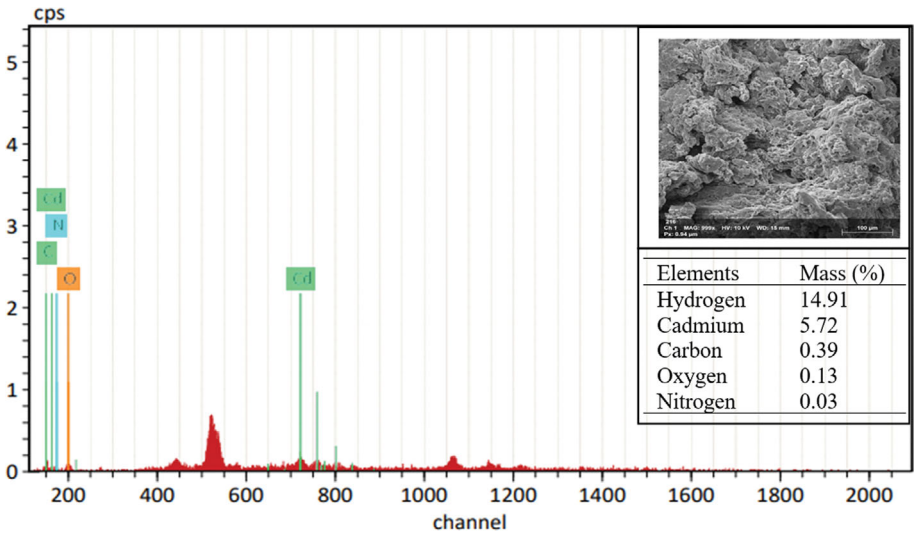

Fig. 3. EDX elemental distribution mapping for SAHs.

tributed elements.

3-4. Surface Crystallinity Studies

The XRD patterns of the native corn starch, poly(AN)-g-starch, superabsorbent hydrogel (SAHs) and cadmium-loaded SAHs are presented in Fig. 4. The native corn starch (Fig. 4(a)) was regarded as a semi-crystalline polymer due to the presence of two broad char-

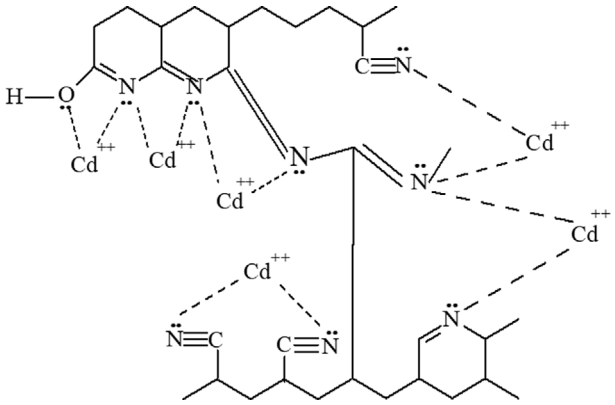

Scheme 1. Proposed complex structure between superabsorbent hydrogel (SAHs) and Cd(II) ions.

acteristic peaks at 2θ=13.03° (with d-spacing 6.79 Å and 72.30% relative intensity) and 20.03° (with d-spacing 4.43 Å and 100% relative intensity). Meanwhile, Fig. 4(b) (XRD diffractogram of poly (AN)-g-starch) shows an increased crystallinity due to the grafting effect. Thus, a single narrow peak was identified at 16.87° (with d-spacing 5.25 Å and 100% relative intensity). This peak could be linked to the polyacrylonitrile grafting since the thermally unstable crystalline structure of the starch could have been destroyed at the high grafting temperature of 85 °C.

In Fig. 4(c), the alkaline hydrolysis (formation of hydrogel) caused a further collapse in the sample structural crystallinity. The poly (AN)-g-starch charge neutralization caused by the saponification agent (NaOH) and the subsequent precipitation of the hydrogel (SAHs) led to a coacervation-phase inversion. Thus, the observed crystalline peak in Fig. 4(b) literally disappeared and paved the way for the existence of wide pseudo - maxima peaks at 2θ=28.33°, 46.53° and 56.12°, while, a long stretch of diffuse reflection region existed afterwards. The formation of metal complexes on SAHs surface after cadmium (II) uptake further resulted in the weakening of the peaks previously observed in the unloaded-SAHs dif- fractogram (Fig. 4(d)). This finding suggests the non-discrete distribution of relatively disordered phase all through the Cd (II)-loaded SAHs structure.

4. The Influence of Process Variables on the Metal Adsorption Process

4-1. The Influence of Solution pH

A preliminary study showed that high operational pH range (pH>5.0) was unfavorable for Cd (II) ion uptake onto SAHs. This could be due to the precipitation of the aqueous metal ion at such a pH range [25]. Hence, the effect of initial pH was varied in the pH range of pH 2.0 to 6.0 at constant adsorbent mass (0.3 g/L), time (20 min) and initial adsorbate concentration (600 mg/L). The generated experimental data was presented in form of a plot in Fig. 5. Consequently, sustained improvement in the Cd (II) ion uptake was observed as the adsorbate solution pH increased (decreasing acidity) from pH 2.0 to pH 5.0. Therefore, the optimum solution pH for maximum Cd (II) ion uptake (536.1 mg/g) was recorded at pH 5.0. Meanwhile, the positively charged nitrogen groups on the SAHs, with their abundant coordination numbers (see Scheme 1), provided veritable chelation sites (via the donation of electron lone pairs) for cadmium ion binding through the

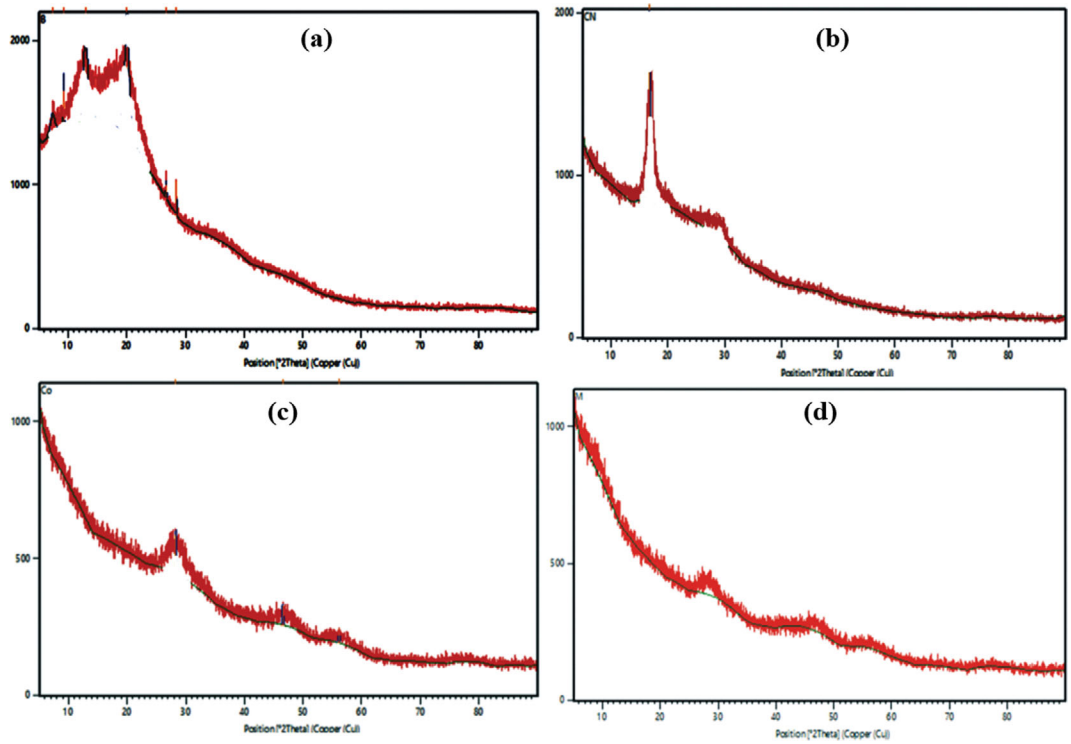

Fig. 4. The XRD diffractogram of (a) native corn starch, (b) poly(AN)-g-starch, (c) hydrolyzed poly(AN)-g-starch, (d) Cd (II)- loaded-hydrolyzed poly(AN)-g-starch.

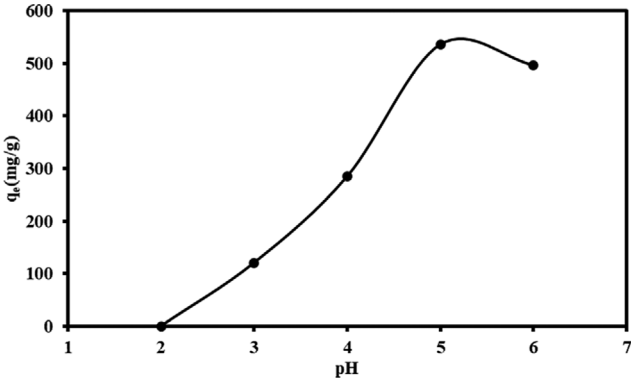

Fig. 5. A plot of the influence of solution pH on SAHs adsorption capacity.

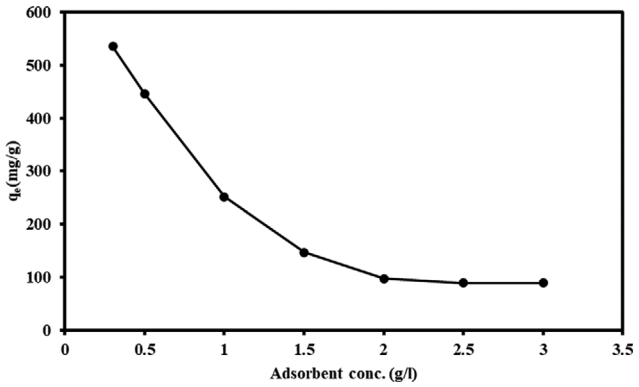

Fig. 6. The influence of adsorbent dose on the cadmium ion adsorption capacity.

formation of metal complexes. This assertion was further elaborated in the Cd (II) ion adsorption mechanism discussion presented in section 3.6. Hence, metal complexation is fingered as the predominant mechanism involved in the Cd (II) ion uptake by SAHs. Furthermore, a significant decline in uptake capacity, from 536.1 mg/g (at pH 5.0) to 496.17 mg/g (at pH 6.0) was observed. At such a higher pH range, Basri et al. [25] reported the precipitation of the aqueous metal ions, and this could explain the observed decline in uptake capacity when the solution pH increases beyond pH 5.0 (Fig. 5).

4-2. The Influence of Adsorbent Dosage

During the study, the contact time, solution pH and initial adsorbate concentration were kept constant at 20 min, pH 5.0 and 600 mg/L. Meanwhile, the experimental finding on the influence of SAHs amount on its cadmium ion uptake is presented as a plot in Fig. 6. A dual-staged regime could be observed in the plot in Fig. 6. The initial stage with a sharp decline in the amount of Cd (II) ion adsorbed was observed after an increase in the adsorbent mass from 0.3 to 1.5 g/L, with a corresponding decrease in uptake amount from 535.22 to 146.53 mg/g, respectively. This observation could be due to a reduction in the amount of initially available chelation sites occasioned by possible chelation site clogging and overcrowding. Furthermore, steady and uniform abating of the Cd (II) ion uptake amount, irrespective of the adsorbent mass, characterized the second regime of the plot (the regions beyond the 1.5 g/L adsorbent dose). At that regime, the SAHs uptake performance was no longer a function of the chelation site availability due to the establishment of an equilibrium relationship between adsorbed cadmium ions and that in the bulk adsorbate phase. Findings by Basri et al. [25] and Singanan et al. [67] corroborate the result reported in this work. Hence, an optimum SAHs mass of 0.3 g/L was adopted.

5. Adsorption Modelling

5-1. The Influence of Contact Time and Kinetic Studies

The study of the influence of contact time is important for elucidating the different kinetics involved in the sorption process and provides useful developmental information for the design of an economically viable water treatment set-up [25]. The influence of contact time in the range of 0 to 300 min was investigated during the cadmium ion uptake. A rapid equilibrium time of 20 min was recorded for both 200 and 600 mg/L initial metal ion concentration. At this initial adsorption stage, the chelation sites were mostly unsaturated/unoccupied, hence the observed rapid cadmium ion adsorption rate.

The obtained kinetic related data was further modelled using the pseudo-first-order, pseudo-second-order, Elovich, intraparticle diffusion and Bangham kinetic models. The theoretical background and the mathematical expression of the respective kinetic models

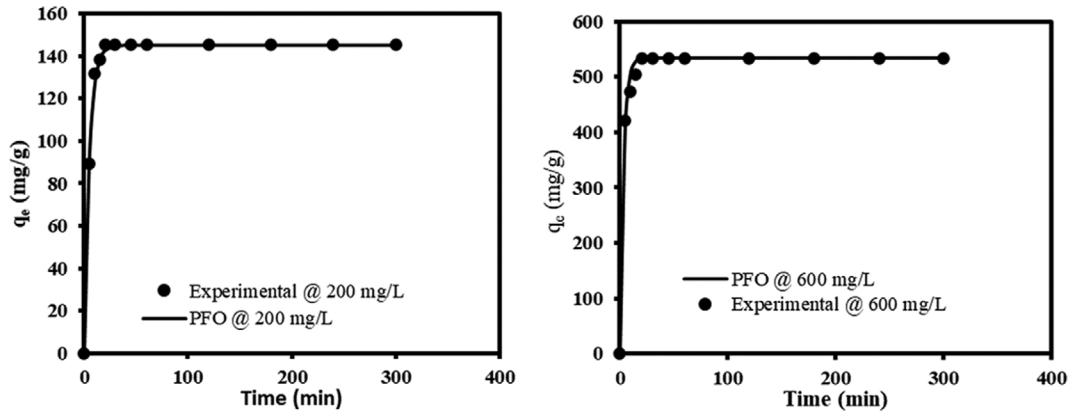

Fig. 7. The pseudo-first-order plot for 200 mg/L and 600 mg/L adsorption system.

Table 3. Kinetic model parameters

Pseudo-first order	Pseudo-second order	Elovich	Bangham	Intra-particle diffusion
200 mg/L				
q_e=145.261	q_e=146.655	α=13.506	q_e=145.260	k_{id}=−7.8E-06
k_1=0.205	k_2=0.006	β=57.843	k_b=0.065	C=145.260
R^2= 0.999	R^2=0.995	R^2=0.990	n=1.561	R^2=0.984
			R^2=0.999	
600 mg/L				
q_e=534.045	q_e=540.173	α=100.00	q_e=533.860	k_{id}=0.517
k_1=0.309	k_2=0.001	β=42.855	k_b=0.039	C=526.922
R^2=0.999	R^2=0.999	R^2=0.994	n=2.287	R^2=0.994
			R^2=0.998	

NB: $q_{e,exp}$=533.86 mg/g (for 600 mg/L system) and 145.13 mg/g (for 200 mg/L system)

were elaborately presented in section 2.6. The import of the respective model parameters to the present adsorption system at different initial adsorbate concentrations (200 and 600 mg/L) was subsequently discussed.

5-1-1. Pseudo-first Order Model

The pseudo-first-order (PFO) model's plot and the parameters obtained at 200 and 600 mg/L are presented in Fig. 7 and Table 3, respectively. Relatively high values (>0.99) of the coefficient of determination (R^2) were obtained at all adsorbate concentrations, an indication of the good fit of the PFO model. The PFO adsorption rate constant (k_1) value was found to increase as the initial adsorbate concentration. Also, the modelled values of maximum adsorption capacity ($q_{e,Cal}$) for both the 200 ($q_{e,Cal}$=534.05 mg/g) and 600 mg/L ($q_{e,Cal}$=145.26 mg/g) adsorption systems are consistent with the experimentally derived uptake amount ($q_{e@200\,mg/L}$=145.13 mg/g and $q_{e@600\,mg/L}$=533.86 mg/g). This consistency in the $q_{e,Cal}$ and $q_{e,Exp}$, which was further confirmed via curve fitting as shown in Fig. 7 is an indication for the PFO model prediction adequacy.

5-1-2. Pseudo-second Order Model

The pseudo-second-order (PSO) model also showed a reasonably good fit to the experimental data (R^2>0.99) (Table 3 and Fig. 8), but its model fit is slightly inferior to that of the PFO. Unlike the k_1-value, the PSO rate constant (k_2) decreased with increasing initial adsorbate concentration. Similarly, the modelled adsorption capacity for both adsorption systems was well consistent with the experimentally derived adsorption capacity (Table 4) and was found to increase with initial adsorbate concentration. Such an increase could be attributed to the propensity of the Cd (II) ions to migrate from the bulk phase to the solid phase with increasing initial concentration. A similar result was reported by Zhuang et al. [68] and Menkiti et al. [69].

5-1-3. Elovich Model

Elovich model depicted some high R^2-values (R^2≥0.99) (Table 3), thus showing the high possibility for its good fitting to the experimental data. However, evaluation of its curve fitting as presented in Fig. 9 showed a wide deviation of the modelled curve line from the experimental data point. Furthermore, its initial adsorption rate (α) varied significantly with initial adsorbate concentration, as it increased from 13.51 (200 mg/L system) to 100.0 mg/g/min (600 mg/L system) (Table 3). Also, the desorption constant values were outrageously large (>40 g/mg), thus confirming the model's poor fit to the experimental data.

5-1-4. Bangham Model

Bangham's kinetic model showed a good fit to the experimental data with R^2 values ≥0.98 at all concentrations studied (Fig. 10). The high R^2 values (Table 3) suggest the occurrence of some degree

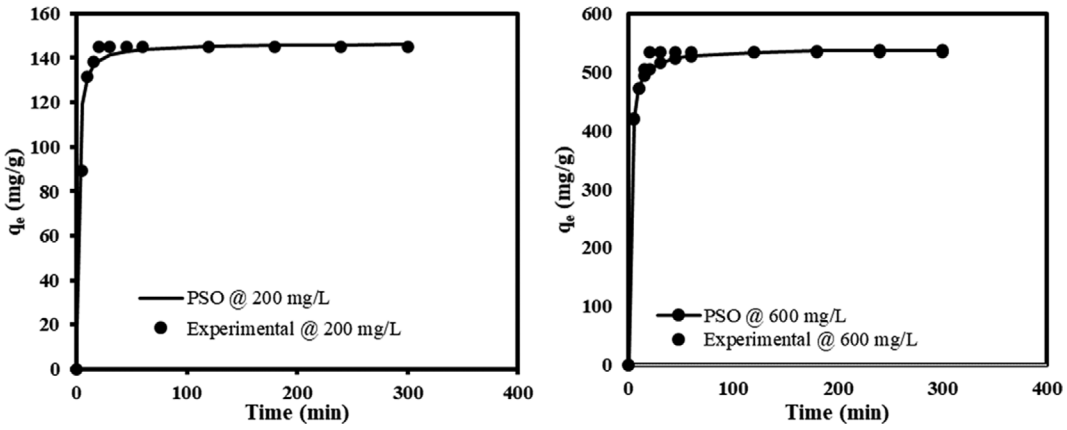

Fig. 8. The pseudo-second-order plot for 200 mg/L and 600 mg/L adsorption system.

Table 4. Error-values for kinetic modelling

Pseudo-first order	Pseudo-second order	Elovich	Bangham	Intra-particle diffusion
200 mg/L				
ARE=0.099	ARE=0.463	ARE=1.055	ARE=0.143	ARE=0.780
APE=0.899	APE=4.211	APE=9.591	APE=1.297	APE=7.090
EABS=11.489	EABS=48.461	EABS=137.547	EABS=14.584	EABS=76.460
ERRSQ=44.906	ERRSQ=965.693	ERRSQ=2207.4	ERRSQ=114.031	ERRSQ=3365.444
Hybrid=0.388	Hybrid=10.497	Hybrid=17.485	Hybrid=1.176	Hybrid=36.821
MPSD=0.003	MPSD=0.115	MPSD=0.146	MPSD=0.012	MPSD=0.406
X^2=0.390	X^2=8.013	X^2=15.870	X^2=1.287	X^2=23.168
SNE=1.2954	**SNE=1.0743**	**SNE=1.0823**	**SNE=1.1622**	**SNE=1.0430**
600 mg/L				
ARE=0.129	ARE=0.161	ARE=0.662	ARE=0.187	ARE=0.458
APE=1.171	APE=1.463	APE=6.024	APE=1.701	APE=4.161
EABS=62.663	EABS=85.100	EABS=348.068	EABS=90.254	EABS=206.700
ERRSQ=1915.564	ERRSQ=1501.364	ERRSQ=15882.92	ERRSQ=4493.784	ERRSQ=15350.85
Hybrid=3.973	Hybrid=2.827	Hybrid=29.939	Hybrid=9.389	Hybrid=35.452
MPSD=0.008	MPSD=0.005	MPSD=0.056	MPSD=0.020	MPSD=0.082
X^2=3.718	X^2=2.954	X^2=28.476	X^2=8.421	X^2=29.062
SNE=1.0374	**SNE=1.0616**	**SNE=1.0260**	**SNE=1.0244**	**SNE=1.0180**

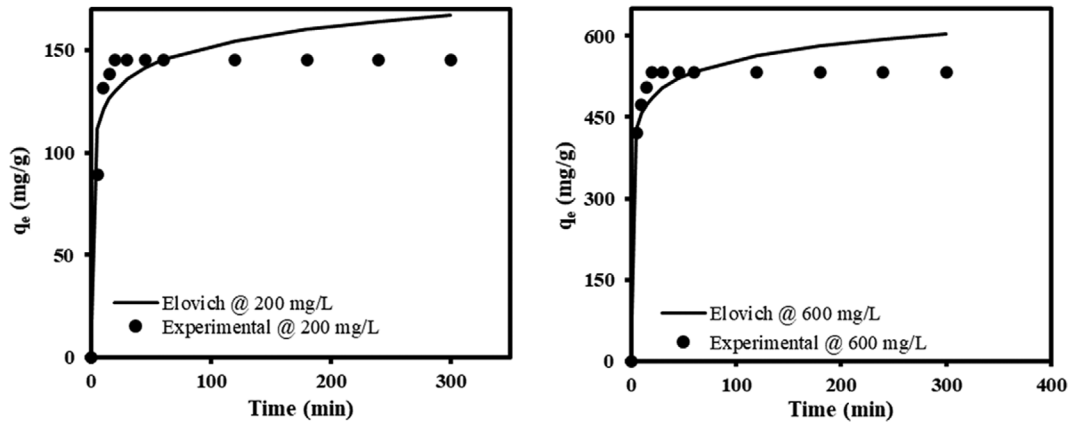

Fig. 9. The Elovich plot for 200 mg/L and 600 mg/L adsorption system.

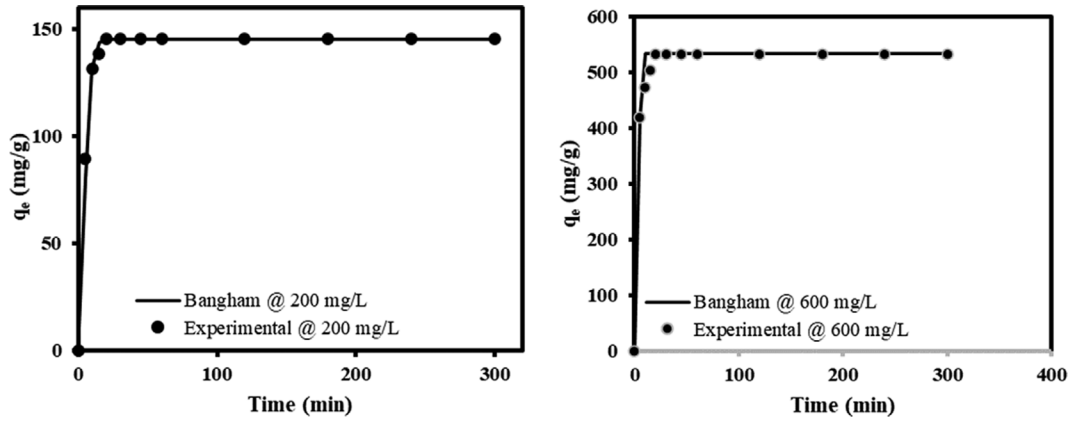

Fig. 10. The Bangham plot for 200 mg/L and 600 mg/L adsorption system.

of pore diffusion, which cannot be regarded as the rate-limiting step in the adsorption process. A variation of the Bangham's parameters (k_b, q_e and n) with initial adsorbate concentration was also observed. The value of k_b decreased from 0.065 to 0.039 mL/g/L, while the 'n-value' increased from 1.56 to 2.29 for the 200 and 600 mg/L adsorption system, respectively. The consistent trend of parametric result recorded, coupled with the good correlation that existed between the experimental and Elovich model curve line (Fig. 10), indicated the model's good fit.

5-1-5. Intraparticle Diffusion Model

The intraparticle diffusion model provides insight into the dependence of mass transfer resistance in a given adsorbent to its adsorption capacity. The model's plot and the obtained parametric values are presented in Fig. 11 and Table 3, respectively. The coefficient of determination values was greater than 0.9 for both the adsorption system. However, the intraparticle diffusion rate constant (k_{id}) for the 200 mg/L adsorption system had a negative value, a development which informed of the model's inability to efficiently predict such adsorption system. Furthermore, the boundary layer effect was hugely predominant in both adsorption systems, judging from the large c-values of 145.26 and 526.92, as a large c-value implies greater boundary layer effect [61,70]. Therefore, intraparticle diffusion cannot be regarded as a probable sorption mechanism in the study.

5-1-6. Application of Error Function in the Determination of the Model of Best Fit

In this study, the application of the seven error functions (see Table 1) produced different error values for the respective kinetic models. It was, however, observed that a given model which recorded a small error value in some error models could depict a very large value for another error model. Therefore, to circumvent the obvious ambiguity associated with the error values inconsistency from one error model to another and to perform a meaningful comparison between the kinetic models, a procedure of normalizing and combining the error results was adopted. This procedure involved the division of all the error values obtained for the different error function models (for a given kinetic model), with the lowest error value and their subsequent summation to generate the minimum normalization error, SNE [54,71]. Hence, the model with the lowest SNE-value is considered the best fit [54]. The error values and the sum of normalized error (SNE) recorded for all the kinetic models are presented in Table 4. The intraparticle diffusion model, having the lowest SNE values of 1.0180 and 1.043, emerged as the best fit model for cadmium ion adsorption for 600 and 200 mg/L

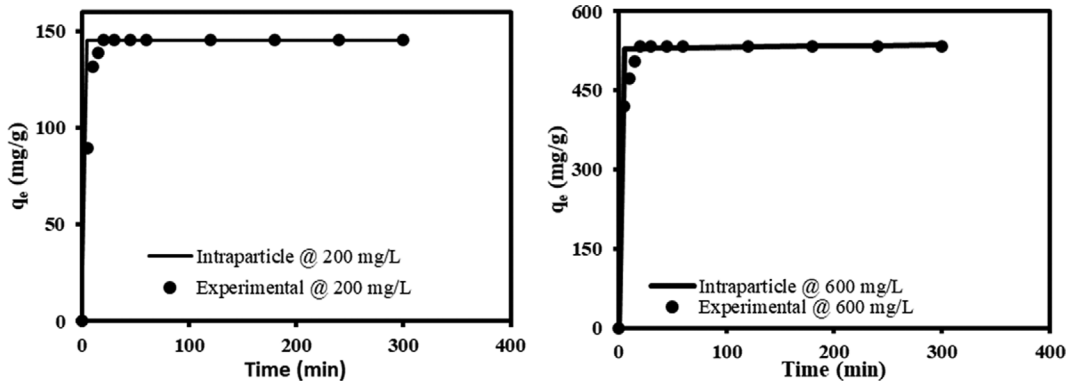

Fig. 11. The Intraparticle diffusion plot for 200 mg/L and 600 mg/L adsorption system.

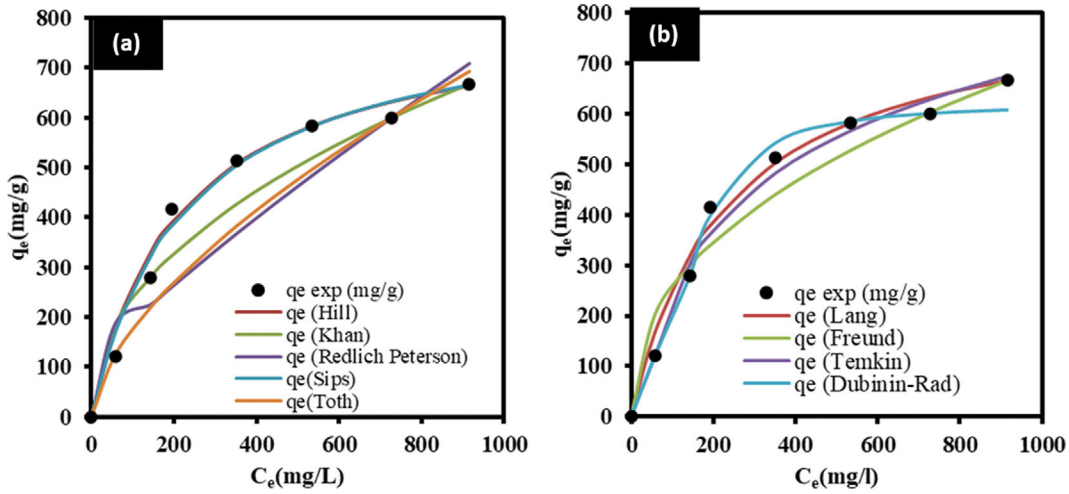

Fig. 12. The isotherm plots for (a) 3-parameter (b) 2-parameter models.

system, respectively.

5-2. Isotherm Studies

Information about the isothermal behavior of Cd (II) ions was determined from the effect of initial adsorbate concentration. The uptake efficiency generally increased correspondingly as the initial adsorbate concentration. The adsorbate concentration effect of the equilibrium adsorption data was fitted to four different 2-parameter and other five 3-parameter models. The theoretical background and the mathematical expression of the models are presented in section 2.5. Similarly, the associated isotherm model plots and obtained parameters are presented in Fig. 12 and Table 5, respectively. For nonlinear modelling, Abonyi et al. [72] reported the insufficiency of only R^2-value as a means of selecting the model of best fit. Incidentally, all the isotherm models depicted very high R^2-values ($R^2 \geq 0.9$) (Table 5), and such ambiguity makes the identification of the model of best fit very clumsy. Therefore, seven error models (see Table 1) which produced different error values for the respective kinetic models were applied. As already explained in the previous paragraph, a procedure of normalizing and combining the error results was adopted to limit the ambiguity associated with the error values inconsistencies. The suitability of a particular model was determined mostly by the sum of normalized error (SNE) values. The lower the SNE value, the greater the associated model appropriateness and adequacy for explaining the

Table 5. Isotherm model parameters

2-Parameter models				
Langmuir	Freundlich	Temkin	D-R*	
q_{max}=834.53	n_F=2.32	A_T=0.03	q_D=618.99	
K_L=3.61	K_F=35.19	b_T=12.57	β_D=0.003	
R_L=0.004	R^2=0.987	R^2=0.997	R^2=0.997	
R^2=0.996				
3-Parameter models				
Khan	R-P*	Sips	Toth	Hills
$q_{k\,max}$=1.808	k_g=0.053	K_S=3.838	k_T=10.070	q_{SH}=830.045
b_K=0.531	α_R=−1.066	α_S=0.005	α_T=0.090	n_H=0.970
α_K=329.070	g=−0.020	β_S=0.990	1/t=0.380	K_H=188.144
R^2=0.984	R^2=0.956	R^2=0.996	R^2=0.965	R^2=0.995

*D-R=Dubinin-Radushkevich; R-P=Redlich-Peterson

Table 6. Error-values for isotherm modelling

2-Parameter models				
Langmuir	Freundlich	Temkin	D-R*	
ARE=0.690	ARE=1.171	ARE=0.359	ARE=0.194	
APE=9.855	APE=16.734	APE=5.125	APE=2.774	
EABS=165.869	EABS=307.354	EABS=160.131	EABS=107.303	
ERRSQ=6255.095	ERRSQ=20977.39	ERRSQ=5492.241	ERRSQ=4648.405	
Hybrid=28.764	Hybrid=85.956	Hybrid=12.567	Hybrid=7.618	
MPSD=0.180	MPSD=0.528	MPSD=0.030	MPSD=0.013	
X^2=23.265	X^2=68.556	X^2=13.526	X^2=8.082	
SNE=1.0366	**SNE=1.0229**	**SNE=1.0349**	**SNE=1.0271**	
3-Parameter models				
Khan	R-P*	Sips	Toth	Hill
ARE=1.027	ARE=1.644	ARE=0.716	ARE=1.060	ARE=0.789
APE=14.671	APE=23.486	APE=10.231	APE=15.150	APE=11.273
EABS=308.930	EABS=565.675	EABS=167.852	EABS=461.066	EABS=175.361
ERRSQ=24196.86	ERRSQ=64920.19	ERRSQ=6598.28	ERRSQ=52330.37	ERRSQ=7600.445
Hybrid=75.034	Hybrid=167.716	Hybrid=31.552	Hybrid=116.53	Hybrid=39.813
MPSD=0.360	MPSD=0.600	MPSD=0.201	MPSD=0.271	MPSD=0.265
X^2=73.843	X^2=212.602	X^2=24.922	X^2=166.070	X^2=29.703
SNE=1.0196	**SNE=1.0150**	**SNE=1.0357**	**SNE=1.0145**	**SNE=1.0338**

*D-R=Dubinin-Radushkevich; R-P=Redlich-Peterson

experimental data.

Table 6 presents the error values and SNE for all the kinetic models. The R-P and Toth mode jointly depicted the lowest SNE values of 1.0150 and 1.0145, respectively, thus the best fit model. The Dubinin-Radushkevich isotherm is often employed in distinguishing the nature of the process: whether physical (E<8 KJ/mol) or chemical (E>8 KJ/mol) [73]. The magnitude of the D-R mean energy, E (12.91 KJ/mol), as evaluated from Eq. (14), is larger than 8 kJ/mol. This suggests the occurrence of unfavorability of electrostatic interaction (which was confirmed in section 3.4.1 and section 3.6) mechanism during Cd (II) ion uptake and a high possibility of the dominance of chemisorption [74,75].

The maximum adsorption capacity for the Langmuir model was much higher than the experimental adsorbed amount and this is an unacceptable development; thus the model is unfit for modelling the present experimental data. Also, the favorability index (R_L) of the cadmium ion uptake was evaluated from Eq. (12), where K_L is the Langmuir constant and C_o is the initial concentration of the adsorbate in solution. The calculated R_L-value of 0.004 (Table 5) was less than 1 and greater than zero, thus indicating a favorable adsorption process. The Freundlich constant (n) signifies the affinity of an adsorbate for an adsorbent. Its value was found to be greater than unity, thus signifying favorable adsorption [76] and the physical nature of the adsorption process. The Temkin isotherm b_T constant is related to the adsorption energy variation. A positive value of the b_T constant depicted in Table 5 indicates the favorability of low temperature during Cd (II) ion adsorption. The magnitude of the R-P exponent (g) suggests the homogeneity or otherwise of an adsorption system [16]. The negative g-values obtained in the study (which is tending to zero) suggest heterogeneous adsorption.

6. Adsorption Mechanism

The oxygen-based and nitrogen-based (amide, nitrile, etc.) functional groups, which were identified from the FTIR and EDX elemental mapping, provided several important metal ion binding sites**.** During the sorption process, the Cd (II) ion depicted large coordination numbers, while chelating with the oxygenous and nitrile functional groups as shown in Scheme 1. The benefits of these important functional groups were so pronounced, as each of the respective oxygen and nitrogen atoms offered a lone pair of electrons for the formation of metal complexes (Scheme 1). Therefore, the occurrence of metal complexation as the predominant sorption mechanism is postulated in the study.

CONCLUSIONS

The gelatinization, copolymerization grafting and saponification (hydrogel formation) of the corn starch afforded the superabsorbent hydrogels (SAHs) adsorbent used in the study. The study on the effect of process variables during the metal adsorption process (via batch mode) showed that SAHs gave an optimal sorption performance at pH 5.0, under a fast equilibrium time of 20 min. The Langmuir maximum adsorption capacity of 834.53 mg/g was recorded in the study. This value showed a wide variation from the experimentally derived maximum adsorption capacity value of 533.86 mg/g and, hence, renders the model unfit for this study. Meanwhile, the Toth and intraparticle diffusion models satisfactorily predicted the isotherm and kinetic data, respectively. Therefore, with a demonstrable fast uptake and high sorption performance (due to the presence of important chelation functional groups), SAH is a suitable and efficient adsorbent for aqueous cadmium ion sequestration.

DATA AVAILABILITY STATEMENT

The raw/processed data required to reproduce these findings cannot be shared at this time as the data also forms part of an ongoing study.

REFERENCES

1. M. G. Sajilata, R. S. Singhal and P. R. Kulkarni, *Comprehensive Rev. Food Sci. Food Saf.*, **5**(1), 1 (2006).
2. R. F. Tester, J. Karkalas and X. Qi, *J. Cereal Sci.*, **39**(2), 151 (2004).
3. H. Ismail, M. Irani and Z. Ahmad, *Int. J. Polym. Mater. Polym. Biomater.*, **62**(7), 411 (2013).
4. E. M. Ahmed, *J. Adv. Res.*, **6**(2), 105 (2015).
5. A. Smart, B. de Lacy Costello, P. White, M. Avison, C. Batty, C. Turner, R. Persad and N. Ratcliffe, *J. Pharm. Biomed. Anal.*, **167**, 59 (2019).
6. A. Hashem, A. Fletcher, H. Younis, H. Mauof and A. Abou-Okeil, *Int. J. Biol. Macromol.*, **164**, 3193 (2020).
7. A. Hashem, S. Badawy, S. Farag, L. Mohamed, A. Fletcher and G. Taha, *J. Environ. Chem. Eng.*, **8**(4), 103966 (2020).
8. S. Zaccaron, U. Henniges, A. Potthast and T. Rosenau, *Carbohydr. Polym.*, **240**, 116251 (2020).
9. A. Hashem, A. Azzeer and A. Ayoub, *Polym.-Plast. Technol. Eng.*, **49**(14), 1463 (2010).
10. A. Hashem, A. Fletcher, M. El-Sakhawy, L. A. Mohamed and S. Farag, *J. Polym. Environ.*, **28**(9), 2498 (2020).
11. G. Yan, B. Chen, X. Zeng, Y. Sun, X. Tan and L. Lin, *Carbohydr. Polym.*, **244**, 116492 (2020).
12. E. S. Abdel-Halim and A. A. Al-Hoqbani, *BioResources*, **10**(2), 3112 (2015).
13. A. Hashem, H. A. Hussein, M. A. Sanousy, E. Adam and E. E. Saad, *Polym.-Plast. Technol. Eng.*, **50**(12), 1220 (2011).
14. F. Gao, D. Li, C.-h. Bi, Z.-h. Mao and B. Adhikari, *Carbohydr. Polym.*, **103**, 310 (2014).
15. C. Noè, C. Tonda-Turo, A. Chiappone, M. Sangermano and M. Hakkarainen, *Polymers*, **12**(6), 1359 (2020).
16. C. O. Aniagor and M. C. Menkiti, *Sigma*, **38**(3), 1073 (2020).
17. A. Hashem, A. Abou-Okeil, A. El-Shafie and M. El-Sakhawy, *Polym.-Plast. Technol. Eng.*, **45**(1), 135 (2006).
18. A. Hashem, *Polym.-Plast. Technol. Eng.*, **45**(1), 35 (2006).
19. A. Hashem, E. Abdel-Halim, K. F. El-Tahlawy and A. Hebeish, *Adsorpt. Sci. Technol.*, **23**(5), 367 (2005).
20. A. Hashem, M. Afifi, E. El-Alfy and A. Hebeish, *Am. J. Appl. Sci.*, **2**(3), 614 (2005).
21. A. Hashem, A. Al-Anwar, N. M. Nagy, D. M. Hussein and S. Eisa, *Green Processing and Synthesis*, **5**(2), 213 (2016).
22. L. Ekebafe, D. Ogbeifun and F. Okieimen, *African J. Environ. Sci. Technol.*, **6**(7), 275 (2012).

23. M. Dai, Y. Liu, B. Ju and Y. Tian, *Bioresour. Technol.*, **294**, 122192 (2019).
24. F. N. Muya, C. E. Sunday, P. Baker and E. Iwuoha, *Water Sci. Technol.*, **73**(5), 983 (2016).
25. S. N. Basri, N. Zainuddin, K. Hashim and N. A. Yusof, *Carbohydr. Polym.*, **138**, 34 (2016).
26. G. Güçlü, E. Al, S. Emik, T. B. İyim, S. Özgümüş and M. Özyürek, *Polym. Bull.*, **65**(4), 333 (2010).
27. Z. S. Pour and M. Ghaemy, *RSC Adv.*, **5**(79), 64106 (2015).
28. J. Kuang, K. Y. Yuk and K. M. Huh, *Carbohydr. Polym.*, **83**(1), 284 (2011).
29. C. Wang, X. Li, J. Chen, G. Fei, H. Wang and Q. Liu, *J. Appl. Polym. Sci.*, **122**(4), 2630 (2011).
30. M. Weaver, R. Montgomery, L. Miller, V. Sohns, G. Fanta and W. Doane, *Starch-Stärke*, **29**(12), 413 (1977).
31. N. Taylor and E. Bagley, *J. Appl. Polym. Sci.*, **18**(9), 2747 (1974).
32. C. O. Aniagor, C. A. Igwegbe, J. O. Ighalo and S. N. Oba, *J. Mol. Liq.*, **334**, 116124 (2021).
33. S. N. Oba, J. O. Ighalo, C. O. Aniagor and C. A. Igwegbe, *Sci. Total Environ.*, **780**, 146608 (2021).
34. E. S. Abdel-Halim, *React. Funct. Polym.*, **73**(11), 1531 (2013).
35. C. Aniagor and M. Menkiti, *Appl. Water Sci.*, **9**(4), 77 (2019).
36. Y.-S. Ho and G. McKay, *Process Biochem.*, **34**(5), 451 (1999).
37. W. J. Weber and J. C. Morris, *J. Sanitary Eng. Div.*, **89**(2), 31 (1963).
38. C. Aniagor and M. Menkiti, *J. Environ. Chem. Eng.*, **6**(2), 2105 (2018).
39. A. Hashem, M. Sanousy, L. A. Mohamed, P. U. Okoye and B. Hameed, *J. Polym. Environ.*, **29**(1), 304 (2020)
40. K. Vijayaraghavan, T. Padmesh, K. Palanivelu and M. Velan, *J. Hazard. Mater.*, **133**(1-3), 304 (2006).
41. I. Langmuir, *J. Am. Chem. Soc.*, **38**(11), 2221 (1916).
42. A. W. Adamson and A. P. Gast, *Physical chemistry of surfaces*, Vol. 150, Interscience publishers New York (1967).
43. M. Radushkevich, *Phys. Chem. Sect*, **55**, 331 (1947).
44. A. Günay, E. Arslankaya and I. Tosun, *J. Hazard. Mater.*, **146**(1-2), 362 (2007).
45. A. Dąbrowski, *Adv. Colloid Interface Sci.*, **93**(1-3), 135 (2001).
46. M. Dubinin, *Chem. Rev.*, **60**(2), 235 (1960).
47. M. Temkin, *Acta Physiochim. URSS*, **12**, 327 (1940).
48. N. Ayawei, A. N. Ebelegi and D. Wankasi, *J. Chem.*, 2017, Article ID 3039817 (2017).
49. N. Ayawei, A. Ekubo, D. Wankasi and E. Dikio, *Oriental J. Chem.*, **31**(3), 1307 (2015).
50. R. Farouq and N. Yousef, *Int. J. Chem. Eng. Appl.*, **6**(5), 319 (2015).
51. H. Freundlich, *Z. für Physikalische Chem.*, **57**(1), 385 (1907).
52. J. Toth, *Acta Chim. Hung.*, **69**, 311 (1971).
53. Y. Ho, J. Porter and G. McKay, *Water, Air, Soil Pollut.*, **141**(1-4), 1 (2002).
54. M. Menkiti and C. Aniagor, *Arabian J. Sci. Eng.*, **43**(5), 2375 (2018).
55. O. Redlich and D. L. Peterson, *J. Phys. Chem.*, **63**(6), 1024 (1959).
56. R. K. Prasad and S. Srivastava, *Chem. Eng. J.*, **146**(1), 90 (2009).
57. J. Ng, W. Cheung and G. McKay, *J. Colloid Interface Sci.*, **255**(1), 64 (2002).
58. F. Gimbert, N. Morin-Crini, F. Renault, P.-M. Badot and G. Crini, *J. Hazard. Mater.*, **157**(1), 34 (2008).
59. L. Jossens, J. Prausnitz, W. Fritz, E. Schlünder and A. Myers, *Chem. Eng. Sci.*, **33**(8), 1097 (1978).
60. K. V. Kumar and S. Sivanesan, *J. Hazard. Mater.*, **136**(3), 721 (2006).
61. M. Menkiti, M. Abonyi and C. Aniagor, *Water Conservation Sci. Eng.*, **3**(3), 205 (2018).
62. D. W. Marquardt, *J. Soc. Ind. Appl. Mathematics*, **11**(2), 431 (1963).
63. U. Khair, H. Fahmi, S. Al Hakim and R. Rahim, *J. Phys. Conf. Ser.*, **930**(1), 012002 (2017).
64. A. Kapoor and R. Yang, *Gas Sep. Purif.*, **3**(4), 187 (1989).
65. F. Rivas, F. Beltrán, O. Gimeno, J. Frades and F. Carvalho, *J. Hazard. Mater.*, **131**(1-3), 170 (2006).
66. A.-R. Xu, L. Chen, X. Guo, Z. Xiao and R. Liu, *Int. J. Biol. Macromol.*, **115**, 846 (2018).
67. M. Singanan and E. Peters, *J. Environ. Chem. Eng.*, **1**(4), 884 (2013).
68. S. Zhuang, K. Zhu and J. Wang, *J. Cleaner Prod.*, **285**, 124911 (2020).
69. M. Menkiti, C. Aniagor, C. Agu and V. Ugonabo, *Water Conservation Sci. Eng.*, **3**(1), 33 (2018).
70. N. Kannan and M. M. Sundaram, *Dyes Pigm.*, **51**(1), 25 (2001).
71. K. Y. Foo and B. H. Hameed, *Chem. Eng. J.*, **156**(1), 2 (2010).
72. M. Abonyi, C. Aniagor and M. Menkiti, *Arabian J. Sci. Eng.*, **44**(12), 10017 (2019).
73. A. Dada, A. Olalekan, A. Olatunya and O. Dada, *IOSR J. Appl. Chem.*, **3**(1), 38 (2012).
74. G. Wang, Q. Chang, M. Zhang and X. Han, *React. Funct. Polym.*, **73**(11), 1439 (2013).
75. M. Jiang, W. Yang, Z. Zhang, Z. Yang and Y. Wang, *J. Environ. Sci.*, **31**, 226 (2015).
76. X. Liu, Z.-Q. Chen, B. Han, C.-L. Su, Q. Han and W.-Z. Chen, *Ecotoxicol. Environ. Saf.*, **150**, 251 (2018).